JACS
JOURNAL OF THE AMERICAN CHEMICAL SOCIETY
Article
pubs.acs.org/JACS

Oxide Ion Conductivity in the Hexagonal Perovskite Derivative $Ba_3MoNbO_{8.5}$

Sacha Fop,[†] Janet M. S. Skakle,[†] Abbie C. McLaughlin,*[,†] Paul A. Connor,[‡] John T. S. Irvine,[‡] Ronald I. Smith,[§] and Eve J. Wildman[†]

[†]The Chemistry Department, University of Aberdeen, Meston Walk, Aberdeen AB24 3UE, U.K.
[‡]School of Chemistry, University of St Andrews, St Andrews, Fife KY16 9ST, U.K.
[§]ISIS Facility, Rutherford Appleton Laboratory, Harwell, Didcot OX11 0DE, U.K.

Supporting Information

ABSTRACT: Oxide ion conductors are important materials with a range of technological applications and are currently used as electrolytes for solid oxide fuel cells and solid oxide electrolyzer cells. Here we report the crystal structure and electrical properties of the hexagonal perovskite derivative $Ba_3MoNbO_{8.5}$. $Ba_3MoNbO_{8.5}$ crystallizes in a hybrid of the 9R hexagonal perovskite and palmierite structures. This is a new and so far unique crystal structure that contains a disordered distribution of $(Mo/Nb)O_6$ octahedra and $(Mo/Nb)O_4$ tetrahedra. $Ba_3MoNbO_{8.5}$ shows a wide stability range and exhibits predominantly oxide ion conduction over a pO_2 range from 10^{-20} to 1 atm with a bulk conductivity of 2.2×10^{-3} S cm^{-1} at 600 °C. The high level of conductivity in a new structure family suggests that further study of hexagonal perovskite derivatives containing mixed tetrahedral and octahedral geometry could open up new horizons in the design of oxygen conducting electrolytes.

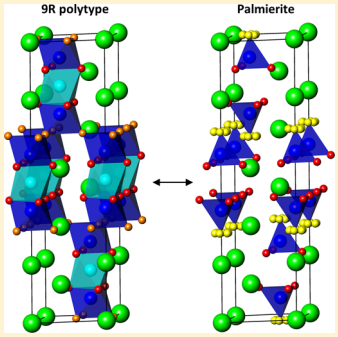

INTRODUCTION

Oxide ion conductors have received much attention in recent years due to their application as electrolytes for solid oxide fuel cells (SOFCs) and solid oxide electrolyzer cells (SOECs), oxygen sensors, and oxygen separation membranes.[1−9] So far several series of fast oxide ion conductors have been reported including fluorite-like systems,[3,6] silicon and germanium apatites,[10] $La_2Mo_2O_9$ (LAMOX) materials,[7] $Bi_4V_2O_{11}$ derivatives,[11] and complex oxides with GaO_4 tetrahedral moieties.[9,12] SOFCs are highly efficient devices that convert chemical energy into electrical energy and require an electrolyte material with specific properties. A good SOFC electrolyte must exhibit negligible electron conductivity, high oxide ion transport, and stability in both oxidizing and reducing atmospheres, as it is in contact with both the anode and cathode sides of the fuel cell. For ease of manufacture and variable-temperature applications, it is desirable to lower the SOFC's operating temperature to an intermediate range (400−600 °C). The oxide ion conductivity of a material is strongly dependent on the crystal structure, and hence in order to reach this objective, it is important to discover and characterize new structural families of oxide ion-conducting materials.

The perovskite family appears to offer great potential for the discovery of new oxide ion conductors due to its capability of adopting numerous structural derivatives. Several perovskite materials with sizable oxide ion conductivity have been reported, including strontium- and magnesium-doped lanthanum gallates (LSGM)[13] and more recently the well-known ferroelectric material $Na_{0.5}Bi_{0.5}TiO_3$.[8] Hexagonal perovskites form when BO_6 octahedra share faces, and different stacking sequences of hexagonal AO_3 layers and the cubic (corner-sharing BO_6 octahedra) and hexagonal (face-sharing BO_6 octahedra) can give rise to a variety of unique crystal structures. There have been accounts of hexagonal systems exhibiting mixed oxide ion and electronic conductivity, but these materials tend to exhibit low conductivities and low transport numbers.[14−16]

Here we report the crystal structure and electrical properties of the hexagonal perovskite derivative $Ba_3MoNbO_{8.5}$. A bulk conductivity of 2.2×10^{-3} S cm^{-1} is observed at 600 °C which is comparable to those of other prominent oxide ion conductors.[1−12] $Ba_3MoNbO_{8.5}$ crystallizes in a hybrid of the 9R hexagonal and palmierite structures.[17,18] The crystal structure contains both $(Mo/Nb)O_6$ octahedra and $(Mo/Nb)O_4$ tetrahedra with intrinsic oxygen vacancies.

EXPERIMENTAL SECTION

$Ba_3MoNbO_{8.5}$ samples were prepared by solid-state reaction of stoichiometric amounts of $BaCO_3$ (99.999%, Aldrich), MoO_3 (99.5+ %, Aldrich), and Nb_2O_5 (99.99%, Aldrich). The starting materials were ground, pressed into a pellet, and calcined in an alumina crucible at 900 °C for 10 h. The pellet was subsequently reground, pelleted, and heated at 1100 °C for 48 h, and then cooled to room temperature at 5 °C/min. The latter heating step was repeated until a phase-pure product was obtained.

Room-temperature X-ray powder diffraction patterns were collected on a PANalytical X'Pert powder diffractometer equipped with a Cu Kα tube. Data were recorded in the range $20° < 2\theta < 70°$, with a step size

Received: October 13, 2016
Published: December 2, 2016

DOI: 10.1021/jacs.6b10730
J. Am. Chem. Soc. 2016, 138, 16764−16769

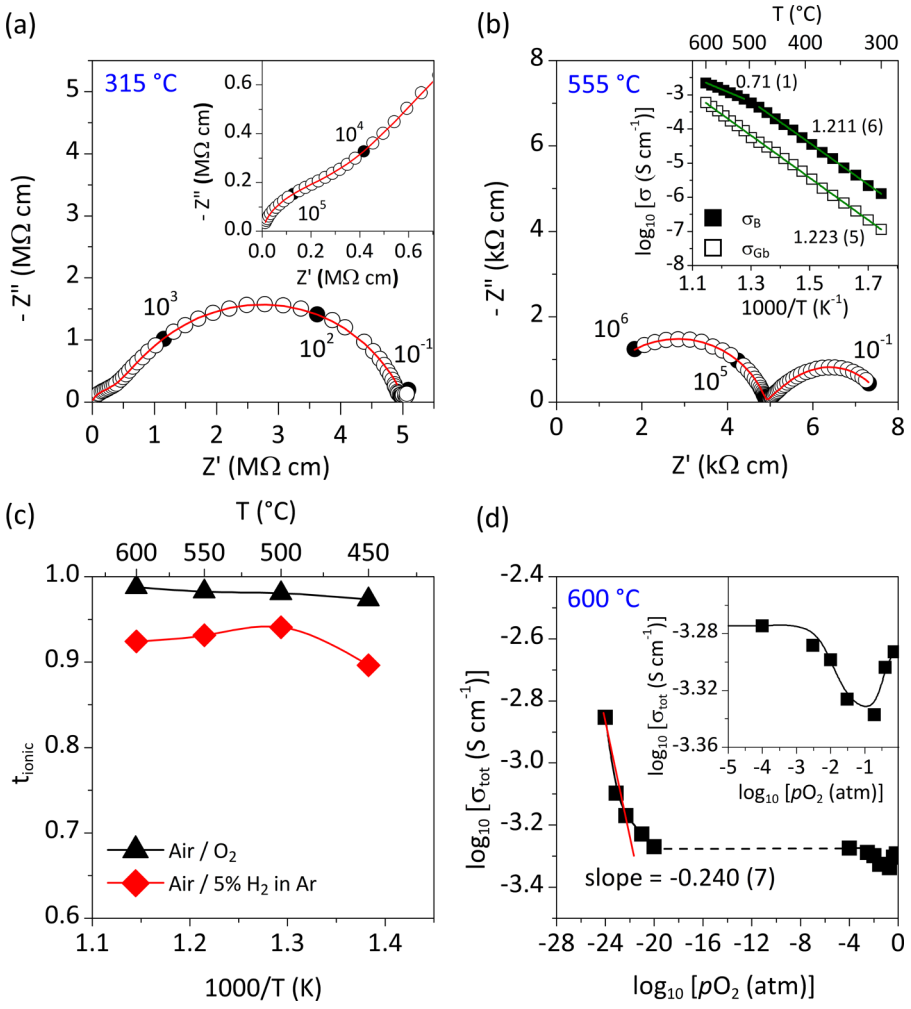

Figure 1. Ionic conductivity of $Ba_3MoNbO_{8.5}$. (a,b) Complex impedance plots recorded in dry air at (a) 315 °C, with inset showing a magnification of the high-frequency data, and (b) 555 °C, with the Arrhenius plot of the bulk and grain boundary conductivity displayed in the inset. (c) Oxygen transport number over the temperature range 450−600 °C measured by the oxygen concentration cell method. (d) Dependence of the total conductivity vs pO_2. The numbers and corresponding filled circles in (a) and (b) indicate selected frequencies (in Hz), while the red line is the equivalent circuit fitting. In the inset to (b), the green line is the linear fit to the data, and the numbers are the activation energies (in eV).

of 0.013°. Time-of-flight (TOF) neutron powder diffraction experiments were performed on the General Material Diffractometer (GEM) at the ISIS spallation source (Rutherford Appleton Laboratory, Harwell, Oxford, UK) at 30 °C on 5 g of $Ba_3MoNbO_{8.5}$ sealed in an 8 mm vanadium can. Data were acquired in the TOF range 500−18 000 μs using the four bank detectors with a total scan time of 2 h.

The oxygen content of $Ba_3MoNbO_{8.5}$ was determined by thermogravimetric analysis in N_2 and O_2 atmospheres using a Stanton Redcroft 780 thermal analyzer. $Ba_3MoNbO_{8.5}$ was heated under an oxygen flow of 50 mL/min from room temperature to 600 °C at 5 °C/min and then held at 600 °C for 14 h. This was then repeated with a nitrogen flow of 50 mL/min.

For the impedance spectroscopy measurements, a pellet of ∼10 mm diameter and ∼1.5 mm thickness was prepared from a powder sample of $Ba_3MoNbO_{8.5}$ and sintered at 1100 °C for 48 h (to achieve >95% of the theoretical density). Pt electrodes were painted on both sides of the pellet using a Pt paste (Metalor 6082). Impedance spectra were recorded with a Solartron 1260 impedance analyzer in the frequency range from 0.1 Hz to 1 MHz with an applied alternating voltage of 0.1 V. Data were recorded upon cooling from 600 to 300 °C in a sealed tube furnace under the flow of dry and moist air, measuring every 15 °C and allowing 2 h of equilibration at each temperature step. The obtained data were corrected by the geometrical factor of the sample and treated with the ZView software (Scribner Associates, Inc.).

Concentration cell measurements were performed on a pellet of $Ba_3MoNbO_{8.5}$ with 97% of the theoretical density. The sample was coated on both faces with Pt paste and cemented on to the holder to ensure gas-tightness. Open-circuit voltages were recorded on cooling from 600 to 450 °C every 50 °C, leaving enough time for the sample to reach equilibrium with the surrounding atmosphere, using a Solartron 1287 electrochemical interface. In all of the measurements one side of the pellet was exposed to a flow of dry air and the other to dry flows of oxygen or a mixture of 5% hydrogen in argon.

The conductivity dependence on the oxygen partial pressure (pO_2) of a porous pellet of $Ba_3MoNbO_{8.5}$ with ∼70% of the theoretical density was recorded at 600 °C over a pO_2 range from 1 to 10^{-27} atm (monitored with a YSZ sensor). The pO_2 range was controlled from 1 to 10^{-4} atm by dilution of O_2 with Ar, and for $<10^{-20}$ atm by 5% H_2 in an argon flow. The conductivity was continuously measured using a Keithley 182 sensitive digital voltmeter with a four-electrode configuration.

RESULTS

Sample Characterization. $Ba_3MoNbO_{8.5}$ has an oxygen stoichiometry between that of the 9R polytype[17] and the palmierite structure.[18] An electron diffraction and high-resolution electron microscopy study previously showed that the oxygen defects with respect to the 9R polytype $(hhc)_3$ leads

DOI: 10.1021/jacs.6b10730
J. Am. Chem. Soc. 2016, 138, 16764−16769

to an ordered distribution of octahedra and tetrahedra in a 3:2 ratio in the cubic layers.[19] The X-ray diffraction pattern of $Ba_3MoNbO_{8.5}$ could be indexed with the space group $R\bar{3}m$ H (a = 5.921(1) Å; c = 21.0908(2) Å), in agreement with previous results,[19] and there was no evidence of impurities. X-ray diffraction data were also recorded after $Ba_3MoNbO_{8.5}$ was annealed at 600 °C for 24 h in flowing O_2, N_2, and 5% H_2/N_2. The X-ray diffraction data show that post annealing there is no change in crystal structure with no evidence of impurities, and that $Ba_3MoNbO_{8.5}$ is stable at temperatures between 20 and 650 °C and at temperatures >1100 °C. $Ba_3MoNbO_{8.5}$ was also annealed in 5% H_2/N_2 at a higher temperature of 1200 °C for 24 h with no evidence of impurity phases in the X-ray diffraction pattern, indicating that $Ba_3MoNbO_{8.5}$ is surprisingly stable in 5% H_2/N_2 (Supplementary Figure 1). The results demonstrate that the $Ba_3MoNbO_{8.5}$ phase presents wider phase stability range under reducing conditions than other leading oxide ion conductors such as LAMOX[20] and the Bi and Ce oxides.[5]

Conductivity of $Ba_3MoNbO_{8.5}$. The electrical properties of a >95% dense pellet of $Ba_3MoNbO_{8.5}$ were measured by a.c. impedance spectroscopy between 300 and 600 °C. A typical impedance spectrum of $Ba_3MoNbO_{8.5}$ recorded in dry air at 315 °C is presented in Figure 1a. An electrode response is observed in the low-frequency region at all temperatures which is indicative of ionic conduction in a material with partially blocking electrodes.[21] The bulk and grain boundary responses are evidenced at higher frequencies with respective capacitance values of $C_B \approx 6.0$ pF cm^{-1} and $C_{Gb} \approx 0.15$ nF cm^{-1}. The complex impedance plots, Z^*, show that the bulk arc is visible at temperatures up to 450 °C. As the temperature increases, the grain boundary arc along with a low-slope electrode element indicative of Warburg type diffusion is observed. At the highest temperatures the electrode response is the main component and turns over as might be expected for finite length Warburg diffusion (Figure 1b). Such evolution is indicative of oxide ion mobility.[21] Furthermore, the electrode response was found to become less resistive when the oxygen content of the atmosphere increased, strongly indicating oxide ion mobility. Equivalent circuit analysis was utilized to extract the individual bulk, grain boundary, and electrode responses at each temperature (see Supporting Information).

The Arrhenius plot of the grain boundary and bulk conductivity of $Ba_3MoNbO_{8.5}$ is presented in Figure 1b. The grain boundaries constitute the most resistive part, thus dominating the total resistivity of the material. The grain boundary conductivity is 5.9×10^{-4} S cm^{-1} at 600 °C with an activation energy of 1.223 ± 0.005 eV. The bulk conductivity is 2.2×10^{-3} S cm^{-1} at 600 °C with an activation energy of 1.211 ± 0.006 eV. A change in slope is evidenced at temperatures >500 °C, with the activation energy lowering to 0.71 ± 0.01 eV. At 600 °C the bulk conductivity is comparable to other leading solid oxide electrolyte materials such as $Na_{0.5}Bi_{0.5}TiO_3$,[8] $Zr_{0.92}Y_{0.08}O_{1.96}$,[22] LAMOX,[7] and $La_{0.9}Sr_{0.1}Ga_{0.9}Mg_{0.1}O_{2.9}$[13] and much greater than perovskite derivatives such as $Ba_2In_2O_5$[23] and $NdBaInO_4$.[24] $NdBaInO_4$ has an ionic conductivity of ~1×10^{-6} S cm^{-1} at 600 °C (Figure 2), although it has recently been shown that it is possible to further enhance the ionic conductivity of $NdBaInO_4$ by substitution of Sr^{2+} for Nd^{3+}; $Nd_{0.9}Sr_{0.1}BaInO_4$ has an ionic conductivity of ~1×10^{-4} S cm^{-1} at 600 °C.[25]

Electromotive force (EMF) measurements using an oxygen concentration cell at selected temperatures between 450 and 600 °C showed oxygen transport numbers of 0.97−0.99 in air/O_2 and 0.90−0.94 in air/5% H_2 in Ar. This suggests that $Ba_3MoNbO_{8.5}$ is an oxide ion conductor with negligible electrical conductivity in air/O_2 and that a small amount of electronic conduction is observed in air/5% H_2 in Ar (Figure 1c). The temperature dependence of the conductivity recorded in a wet air flow resulted in a reduction in both the bulk and total conductivity compared to the same measurement in a dry air flow. This suggests that there is no proton conduction in this material (Supplementary Figure 4). Degradation of the electrical conductivity with time has been seen in other promising oxide ion conductors, for example in the $Bi_4V_2O_{11}$ derivatives.[26] Conductivity data versus time were recorded at 600 °C, and there was no evidence of degradation of the conductivity during the 12 days that the impedance spectra were recorded. (Supplementary Figure 5).

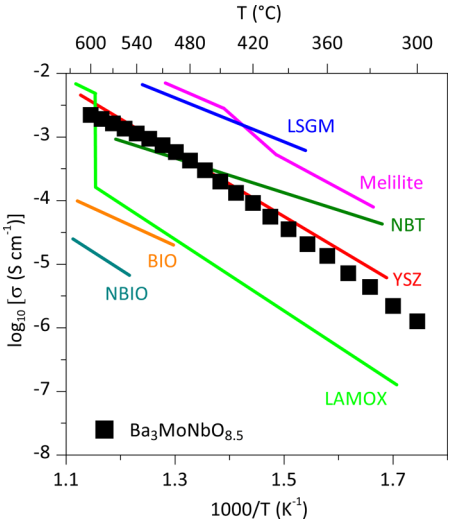

Figure 2. Comparison of bulk conductivities for $Ba_3MoNbO_{8.5}$ and other ionic conductors. Shown are $Zr_{0.92}Y_{0.08}O_{1.96}$ (YSZ, ref 22), $La_{0.9}Sr_{0.1}Ga_{0.8}Mg_{0.2}O_3$ (LSGM, ref 13), $La_2Mo_2O_9$ (LAMOX, ref 7), $Na_{0.5}Bi_{0.5}TiO_3$ (NBT, ref 8), $La_{1.54}Sr_{0.46}Ga_3O_{7.27}$ (Melilite, ref 9), $Ba_2In_2O_5$ (BIO, ref 23), and $NdBaInO_4$ (NBIO, ref 24).

Figure 1d shows the pO_2 dependence of the total conductivity of $Ba_3MoNbO_{8.5}$ at 600 °C. At oxygen partial pressures <10^{-20} atm, an electronic n-type contribution to the total conductivity is evidenced. At oxygen partial pressures <10^{-20} atm, reduction of the Mo^{6+} and/or Nb^{5+} cations results in the formation of oxygen vacancies and electronic defects. The latter exhibit greater mobility than the oxygen vacancies so that the conductivity is dominated by the concentration of the electronic defects, which is proportional to $pO_2^{-1/4}$. The conductivity appears to be independent of oxygen partial pressure over the range from 10^{-20} to 10^{-4} atm. There is evidence of a plateau between $pO_2 = 10^{-20}$ and 10^{-4} atm, indicating oxide ionic conductivity with negligible electronic conduction over this range of pO_2.

Between $pO_2 = 10^{-3}$ and 1 atm, the variation of the total conductivity with oxygen partial pressure is unusual. Upon increasing pO_2 from 10^{-3} to 0.21 atm the total conductivity decreases. As pO_2 increases further from 0.21 to 1 atm, the total conductivity rises, so that there is a minimum in σ_{tot} at pO_2 = 0.21. The transport number recorded in air/O_2 at 600 °C is 0.99. Thermogravimetric analysis data recorded at 600 °C in both flowing N_2 and O_2 showed no significant oxygen gain or loss, suggesting that the presence of the conductivity minimum

DOI: 10.1021/jacs.6b10730
J. Am. Chem. Soc. 2016, 138, 16764−16769

cannot be related to any significant change of the overall phase composition. One possibility is that at $pO_2 > 0.21$ atm the increase in σ_{tot} is a result of a structural change such as a redistribution or ordering of the oxygen vacancies. Variable-temperature neutron diffraction experiments in flowing oxygen, nitrogen, and air will be required to corroborate this. An alternative scenario is that these changes are related to changes in composition at the grain boundary at high temperatures and high pO_2.

Neutron Diffraction. In order to further investigate the crystal structure of $Ba_3MoNbO_{8.5}$, TOF powder neutron diffraction data were recorded at 30 °C on the GEM diffractometer at the ISIS pulsed spallation source. Rietveld refinement[27] of the crystal structure was performed using the GSAS package with the EXPGUI interface.[28,29] The background was fitted by the Chebyschev polynomial function, and the peak shapes were modeled using a pseudo-Voigt function. $Ba_3MoNbO_{8.5}$ has previously been described to have intrinsic oxygen vacancies and intertwined regions of $(Mo/Nb)O_6$ octahedra and $(Mo/Nb)O_4$ tetrahedra.[19] A poor fit to the neutron data was obtained upon using the model previously reported for $Ba_3MoNbO_{8.5}$ in a high-resolution electron microscopy study.

There was no evidence of an ordered distribution of octahedra and tetrahedra within the cubic layers. A poor fit was also obtained to the model previously reported for the stoichiometrically similar compound, $Ba_3VWO_{8.5}$,[30] which contains a purely octahedral coordination of vanadium and tungsten.

Previous electron diffraction[19] and Raman[31] studies had clearly indicated the presence of both $(Mo/Nb)O_6$ octahedra and $(Mo/Nb)O_4$ tetrahedra within the crystal structure. A hybrid model of the palmierite and 9R structures was therefore constructed (Figure 3a, Table 1), and an excellent Rietveld fit to this model is obtained ($\chi^2 = 2.4$, $R_p = 3.29\%$, and $R_{Wp} = 3.24\%$; Figure 4). The oxygen content in $Ba_3MoNbO_{8.5}$ is

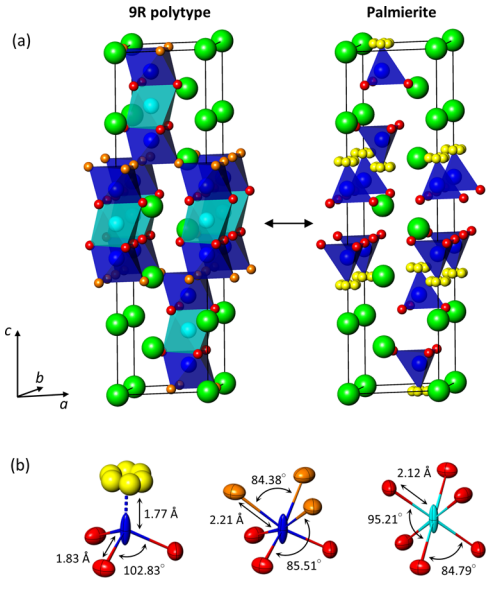

Figure 3. Crystal structure of $Ba_3MoNbO_{8.5}$. (a) The hybrid structural model formed by the superimposition of the 9R polytype and the palmierite subunits representing the average structure of the system. (b) Bond lengths and angles of the $(Mo/Nb)O_4$ tetrahedra and $(Mo/Nb)O_6$ octahedra, with thermal ellipsoids. Colors in (a) and (b): green, Ba(1)/Ba(2); blue, Mo(1)/Nb(1); cyan, Mo(2)/Nb(2); red, O(1); orange, O(2); and yellow, O(3).

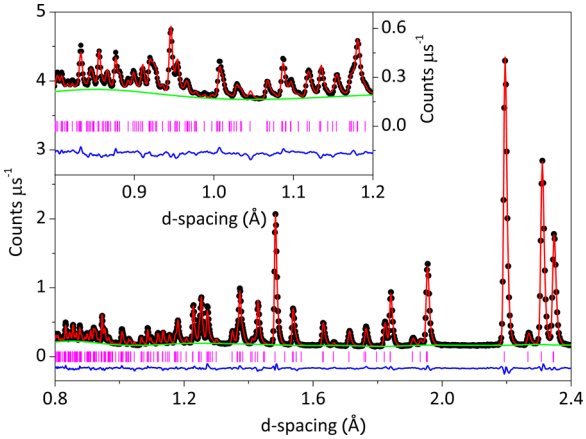

Figure 4. Rietveld refinement fit to the TOF neutron diffraction data of $Ba_3MoNbO_{8.5}$ at 30 °C. Neutron diffraction data from the 91.5° bank detector of the GEM diffractometer is shown. Black dots indicate the observed data, the red line the Rietveld fit, the blue line the difference between the observed and the calculated patterns, the green line the background function, and the pink bars the reflection positions.

intermediate between the two structural types. Both the 9R and the palmierite structures have an $(hhc)_3$ stacking sequence, but oxygen vacancies in the cubic layers of the palmierite $(hhc)_3$ sequence result in the formation of tetrahedral B cations (Figure 3). The oxygen atom at Wyckoff position 18*h* is common to both the 9R and palmierite structures. The palmierite structure also has an oxygen atom at Wyckoff position 6*c* whereas the 9R structure has an oxygen atom at position 9*e*. The hybrid model contains oxygen on all three sites and metals at both the 6*c* and 3*b* Wyckoff positions (Table 1). Refining the oxygen site occupancies results in an overall oxygen stoichiometry of 8.5; the oxygen (O(1)) at position 18*h* is fully occupied, and partial occupancy of O(2) and O(3) is observed (Table 1). Mo^{6+} and Nb^{5+} have very similar relative scattering powers for both X-rays and neutrons, and so it was not possible to determine the ratio of Mo:Nb on each site. It was assumed that the Mo^{6+} and Nb^{5+} cations were disordered over the 6*c* and 3*b* sites. The Ba fractional occupancies refined to within ±1% of the full occupancy and were fixed at 1.0.

The atomic displacement parameters, *U*, were modeled anisotropically for all atoms. The atomic displacement parameters for the two Ba ions were constrained to be the same, as were the atomic displacement parameters for Mo/Nb on the 6*c* and 3*b* sites. Disorder of the oxygen atom, O(3), within the $(Mo/Nb)O_4$ tetrahedra was evidenced by large U_{11}, U_{22}, and U_{12} values. This was modeled by using a single isotropic *U* factor for O(3) and splitting the site as shown in Table 1 and Figure 3. The Ba(2) and Mo(1)/Nb(1) cations and the ideal O(3) 6*c* position are all located on the 3-fold axis, and the Ba(2)−Mo(1)/Nb(1) distance is ∼4.07 Å. It is proposed that the disorder of oxygen onto the 36*i* positions arises as a result of the short distance between Ba(2) and Mo(1)/Nb(1) so that the disorder stabilizes the structure, resulting in longer and more realistic Ba(2)−O(3) and Mo(1)/Nb(1)−O(3) bond lengths. Similar structural disorder has been reported for the mixed conducting hexagonal perovskite $Ba_7Y_2Mn_3Ti_2O_{20}$.[14] The thermal ellipsoids of O(1) and O(2)

DOI: 10.1021/jacs.6b10730
J. Am. Chem. Soc. 2016, 138, 16764−16769

Table 1. Refined Atomic Parameters from Rietveld Fit of the Powder Neutron Diffraction Data Recorded on the GEM Diffractometer at 30 °C[a]

atom	site	x	y	z	occupancy	$U_{11} = U_{22}$ (Å^2)	U_{33} (Å^2)	U_{12} (Å^2)
Ba(1)	3*a*	0	0	0	1	0.0165 (3)	0.0192 (6)	0.0083 (2)
Ba(2)	6*c*	0	0	0.20629 (8)	1	0.0165 (3)	0.0192 (6)	0.0083 (2)
Mo(1)/Nb(1)	6*c*	0	0	0.39936 (6)	0.926 (1)	0.0049 (2)	0.0498 (9)	0.0025 (1)
Mo(2)/Nb(2)	3*b*	0	0	0.5	0.148 (1)	0.0049 (2)	0.0498 (9)	0.0025 (1)
O(1)	18*h*	0.17212 (5)	0.82788 (5)	0.10343 (2)	1	0.0215 (3)	0.0140 (3)	0.0160 (3)
O(2)	9*e*	0.5	0	0	0.449 (2)	0.0240 (8)	0.0121 (3)	0.0155 (4)
O(3)	36*i*	0.0850 (9)	0.0933 (7)	0.3195 (2)	0.096 (1)	0.0342 (2)		

[a]Data were refined in the space group $R\bar{3}m$ H with a = 5.92744 (3) Å, c = 21.0995 (2) Å; χ^2 = 2.4, R_p = 3.29%, and R_{wp} = 3.24%. U_{ij} indicates anisotropic thermal displacement parameters. U_{13} and U_{23} are zero.

and Ba and Mo/Nb atoms are displayed in Figure 3b. The Mo/Nb sites also exhibit highly anisotropic thermal motion ($U_{11} = U_{22}$ = 0.0049(2) Å^2; U_{33} = 0.0498(9) Å^2; U_{12} = 0.0025(1) Å^2). The bond lengths and angles obtained from Rietveld refinement of the crystal structure (Figure 3b; Supplementary Table 1) demonstrate that the $(Mo/Nb)O_6$ and $(Mo/Nb)O_4$ polyhedra are distorted in $Ba_3MoNbO_{8.5}$. Similar bond lengths and angles have been reported for other materials containing mixed tetrahedral/octahedral coordination of Mo and Nb atoms.[32]

DISCUSSION

$Ba_3MoNbO_{8.5}$ is the first hexagonal perovskite derivative to exhibit significant oxide ion conductivity. $Ba_3MoNbO_{8.5}$ crystallizes with an unusual and unique hybrid structure containing a disordered distribution of $(Mo/Nb)O_6$ octahedra and $(Mo/Nb)O_4$ tetrahedra. The crystal structure of $Ba_3MoNbO_{8.5}$ contains intrinsic oxygen vacancies. The O(2) and O(3) sites cannot be simultaneously occupied within the structure of $Ba_3MoNbO_{8.5}$. This leads to the creation of randomly mixed domains of $(Mo(1)/Nb(1))O_6$ octahedra and $(Mo(1)/Nb(1))O_4$ tetrahedra. Locally it is likely that the O(2) and O(3) sites compete for occupation. This would imply that movement of oxide ions is via octahedral and tetrahedral interchange and suggests a cooperative motion such as an interstitialcy mechanism.

A single-crystal X-ray diffraction study has shown that the high oxide ion mobility observed in $La_2Mo_2O_9$[33] is facilitated by the ability of Mo^{6+} to adopt variable coordination environments. The same ability has been reported for Nb^{5+} in the high-temperature structure of the mixed ionic and electronic conductor $Ba_4Nb_2O_9$.[34] It is highly likely that the variable coordination environment for Mo^{6+} and/or Nb^{5+} in $Ba_3MoNbO_{8.5}$ is important for producing a low-energy migration pathway for the oxide ions.

The $(Mo/Nb)O_6$ and $(Mo/Nb)O_4$ polyhedra are also clearly distorted in $Ba_3MoNbO_{8.5}$ (Figure 3b; Supplementary Table 1). It has previously been reported that both d^0 cations Mo^{6+} and Nb^{5+} are susceptible to out-of-center displacement of the metal−oxygen octahedra as a result of a second-order Jahn−Teller distortion.[35] The magnitude of the out of center distortion increases with increasing formal charge and decreases with increasing size of the cation so that a sizable distortion is expected for Mo^{6+}. It is therefore likely that the observed distortions of the $(Mo/Nb)O_6$ and $(Mo/Nb)O_4$ polyhedra, combined with the anisotropic thermal displacement of the Mo/Nb cations and the variable coordination geometry of the Mo^{6+} and/or Nb^{5+} cation, enable facile mobility of the oxide ions through the anion vacancies in the $Ba_3MoNbO_{8.5}$ structure. Further computer modeling is required to establish the diffusion pathways of the oxide ions in $Ba_3MoNbO_{8.5}$.

The bulk ionic conductivity of $Ba_3MoNbO_{8.5}$ at 600 °C is comparable to that of other leading oxide conductors and considerably larger than those reported for other perovskite derivatives such as $NdBaInO_4$ (Figure 2), which exhibits predominantly oxide ion conductivity over the pO_2 range from 3.0×10^{-19} to 3.2×10^{-11} atm.[24] EMF and conductivity versus oxygen partial pressure measurements give evidence that oxide ionic conductivity is observed for $Ba_3MoNbO_{8.5}$ over the pO_2 range from 10^{-20} to 1 atm at 600 °C. The electronic n-type contribution to the total conductivity observed for $pO_2 < 10^{-20}$ is most likely due to the reduction of Mo^{6+} at low pO_2; substitution of Mo^{6+} with the more stable W^{6+} cation could further increase the ionic conduction window, as reported for W-doped LAMOX materials.[20] $Ba_3MoNbO_{8.5}$ exhibits good ionic transport number values of 0.99 in air/O_2 and 0.92 in air/5% H_2 in Ar at 600 °C, which corroborate the results obtained from pO_2 measurements. $Ba_3MoNbO_{8.5}$ is stable under both flowing 5% H_2/N_2 and O_2 and presents a wider stability range under reducing conditions than other leading oxide ion conductors such as the Bi and Ce oxides.[5] There is also no degradation of the electrical conductivity with time and no evidence of proton conduction. Appropriate chemical doping should result in a further increase of the bulk conductivity so that $Ba_3MoNbO_{8.5}$ could be an excellent candidate as an electrolyte for intermediate temperature fuel cells upon further chemical modification. Hexagonal perovskite derivatives containing mixed tetrahedral and octahedral geometry warrant further investigation.

ASSOCIATED CONTENT

Supporting Information

The Supporting Information is available free of charge on the ACS Publications website at DOI: 10.1021/jacs.6b10730.

Experimental data, impedance spectroscopy data fitting, tables of bond lengths and angles, X-ray diffraction patterns, variation of conductivity with time, and impedance spectroscopy data recorded in a moist atmosphere, including Supplementary Figures 1−5 and Supplementary Table 1 (PDF)

AUTHOR INFORMATION

Corresponding Author

*a.c.mclaughlin@abdn.ac.uk

ORCID

Abbie C. McLaughlin: 0000-0001-9960-723X

DOI: 10.1021/jacs.6b10730
J. Am. Chem. Soc. 2016, 138, 16764−16769

Notes

The authors declare no competing financial interest.

■ ACKNOWLEDGMENTS

This research was supported by the Northern Research Partnership and the University of Aberdeen. We also acknowledge STFC-GB for provision of beamtime at ISIS.

■ REFERENCES

(1) Goodenough, J. B. *Annu. Rev. Mater. Res.* **2003**, *33*, 91.
(2) Steele, B.; Heinzel, A. *Nature* **2001**, *414*, 345.
(3) Malavasi, L.; Fisher, C. A. J.; Islam, M. S. *Chem. Soc. Rev.* **2010**, *39*, 4370.
(4) Brett, D. J. L.; Atkinson, A.; Brandon, N. P.; Skinner, S. J. *Chem. Soc. Rev.* **2008**, *37*, 1568.
(5) Wachsman, E. D.; Lee, K. T. *Science* **2011**, *334*, 935.
(6) Kuang, X.; Payne, J. L.; Johnson, M. R.; Radosavljevic Evans, I. E. *Angew. Chem., Int. Ed.* **2012**, *51*, 690.
(7) Lacorre, P.; Goutenoire, F.; Bohnke, O.; Retoux, R.; Laligant, Y. *Nature* **2000**, *404*, 856.
(8) Li, M.; Pietrowski, M. J.; De Souza, R. A.; Zhang, H.; Reaney, I. M.; Cook, S. N.; Kilner, J. A.; Sinclair, D. C. *Nat. Mater.* **2014**, *13*, 31.
(9) Kuang, X.; Green, M. A.; Niu, H.; Zajdel, P.; Dickinson, C.; Claridge, J. B.; Jantsky, L.; Rosseinsky, M. J. *Nat. Mater.* **2008**, *7*, 498.
(10) Kendrick, E.; Islam, M. S.; Slater, P. R. *J. Mater. Chem.* **2007**, *17*, 3104.
(11) Abraham, F.; Debreuille-Gresse, M. F.; Mairesse, G.; Nowogrocki, G. *Solid State Ionics* **1988**, *28-30*, 529.
(12) Kendrick, E.; Kendrick, J.; Knight, K. S.; Islam, M. S.; Slater, P. R. *Nat. Mater.* **2007**, *6*, 871.
(13) Ishihara, T.; Matsuda, H.; Takita, Y. *J. Am. Chem. Soc.* **1994**, *116*, 3801.
(14) Kuang, X.; Allix, M.; Ibberson, R. M.; Claridge, J. B.; Niu, H.; Rosseinsky, M. J. *Chem. Mater.* **2007**, *19*, 2884.
(15) Ling, C. D.; Avdeev, M.; Kutteh, R.; Kharton, V. V.; Yaremchenko, A. A.; Fialkova, S.; Sharma, N.; Macquart, R. B.; Hoelzel, M.; Gutmann, M. *Chem. Mater.* **2009**, *21*, 3853.
(16) Ling, C. D.; Avdeev, M.; Kharton, V. V.; Yaremchenko, A. A.; Macquart, R. B.; Hoelzel, M. *Chem. Mater.* **2010**, *22*, 532.
(17) Durif, A. *Acta Crystallogr.* **1959**, *12*, 420.
(18) Susse, P.; Buerger, M. J. *Z. Kristallogr.* **1970**, *131*, 161.
(19) García-González, E.; Parras, M.; González -Calbet, J. M. *Chem. Mater.* **1998**, *10*, 1576.
(20) Marrero-Lopez, D.; Canales-Vazquez, J.; Ruiz-Morales, J. C.; Irvine, J. T. S.; Nunez, P. *Electrochim. Acta* **2005**, *50*, 4385.
(21) Irvine, J. T. S.; Sinclair, D. C.; West, A. R. *Adv. Mater.* **1990**, *2*, 132.
(22) Kwon, O. H.; Choi, G. M. *Solid State Ionics* **2006**, *177*, 3057.
(23) Goodenough, J. B.; Ruiz-Diaz, J. E.; Zhen, Y. S. *Solid State Ionics* **1990**, *44*, 21.
(24) Fujii, K.; Esaki, Y.; Omoto, K.; Yashima, M.; Hoshikawa, A.; Ishigaki, T.; Hester, J. R. *Chem. Mater.* **2014**, *26*, 2488.
(25) Fujii, K.; Shiraiwa, S.; Esaki, Y.; Yashima, M.; Kim, S. J.; Lee, S. *J. Mater. Chem. A* **2015**, *3*, 11985.
(26) Krok, F.; Malys, M.; Dygas, J. R.; Bogusz, W.; Abrahams, I. *Mol. Phys. Rep.* **2000**, *27*, 46.
(27) Rietveld, H. M. *Acta Crystallogr.* **1967**, *22*, 151.
(28) Larson, A. C.; Von Dreele, R. B. *General Structure Analysis System (GSAS)*; Technical Report No. LAUR86-748, Los Alamos National Laboratory, 2004.
(29) Toby, B. H. *J. Appl. Crystallogr.* **2001**, *34*, 210.
(30) Moessner, B.; Kemmler-Sack, S. *J. Less-Common Met.* **1985**, *114*, 333.
(31) Brown Holden, A. A.; Reedyk, M.; García-González, E.; Parras, M.; Gonzalez-Calbet, J. M. *Chem. Mater.* **2000**, *12*, 2287.
(32) García-González, E.; Parras, M.; González -Calbet, J. M. *Chem. Mater.* **1999**, *11*, 433.
(33) Evans, I. R.; Howard, J. A. K.; Evans, J. S. O. *Chem. Mater.* **2005**, *17*, 4074.
(34) Dunstan, M. T.; Blanc, F.; Avdeev, M.; McIntyre, G. J.; Grey, C. P.; Ling, C. D. *Chem. Mater.* **2013**, *25*, 3154.
(35) Kunz, M.; Brown, D. I. *J. Solid State Chem.* **1995**, *115*, 395.

DOI: 10.1021/jacs.6b10730
J. Am. Chem. Soc. 2016, 138, 16764−16769